Characterization of the sub-mesoscale energy cascade in the Alboran Sea thermocline from spectral analysis of high-resolution MCS data

Valenti Sallares[1], Jhon F. Mojica[1], Berta Biescas[2], Dirk Klaeschen[3], Eulàlia Gràcia[1]

[1] Barcelona-CSI, Institute of Marine Sciences - CSIC, Barcelona, Spain.

[2] Istituto di Scienze Marine - CNR, Bologna, Italy.

[3] GEOMAR Helmholtz Centre for Marine Research, Kiel, Germany.

Corresponding author: Valenti Sallares (vsallares@icm.csic.es)

This article has been accepted for publication and undergone full peer review but has not been through the copyediting, typesetting, pagination and proofreading process which may lead to differences between this version and the Version of Record. Please cite this article as doi: 10.1002/2016GL069782

Abstract

Part of the kinetic energy that maintains ocean circulation cascades down to small scales until it is dissipated through mixing. While most steps of this downward energy cascade are well understood, an observational gap exists at horizontal scales of 10^3-10^1 m that prevents characterizing a key step in the chain: the transition from anisotropic internal wave motions to isotropic turbulence. Here we show that this observational gap can be covered using high-resolution multichannel seismic (HR-MCS) data. Spectral analysis of acoustic reflectors imaged in the Alboran Sea thermocline shows that this transition is likely caused by shear instabilities. In particular, we show that the averaged horizontal wavenumber spectra of the reflectors vertical displacements display three subranges that reproduce theoretical spectral slopes of internal waves [λ_x>100 m], Kelvin-Helmholtz-type shear instabilities [100 m>λ_x>33 m], and turbulence [λ_x<33 m], indicating that the whole chain of events is occurring continuously and simultaneously in the surveyed area.

Key Points:

- High resolution seismic data allows characterizing ocean dynamics at the sub-mesoscale
- Spectral slopes display a transitional subrange between internal waves and turbulence
- The transition is likely driven by shear instabilities of the Kelvin Helmholtz-type

1 Introduction

Ocean kinetic energy is injected in the ocean at the production range by means of the Coriolis force, atmospheric forcing and tides (fig. S1). In a frequency (ϕ) spectrum representation, this subrange represents ocean motions above the Coriolis frequency (f_c), where the main kinematic effect corresponds to the large-scale, geostrophically balanced eddy field. At higher frequencies, motions are described by the meso-scale gravity wave dynamics (fig. S1a), with most energy carried by large-amplitude, near-inertial waves of $f \approx f_c$ [Thorpe, 2005; Müller et al., 2005; Ferrari and Wunsch, 2009]. As they propagate through the ocean, the internal waves transfer their energy to smaller scales through an internal wave continuum driven by scattering and wave-wave interaction processes [Thorpe, 1987, Baines and Mitsudera, 1994]. These processes are thought to continue until the waves reach the buoyancy frequency (N), beyond which they become unstable [McComas and Bretherton, 1977; D'Asaro and Lien, 2000; Carnevale et al., 2001]. Finally, motions at $f > N$ are dominated by small-scale turbulence that follows isotropic internal wave breaking and leads to anisotropic irreversible mixing [e.g. Thorpe, 2005].

While the physics that govern the internal waves and turbulent subranges is now well established, the mechanisms of energy transfer remain poorly understood. The main reason is the lack of observational systems providing synoptic ocean observations in the horizontal direction at the ~10^3-10^1 m range, which is the scale at which the transition between the isotropic internal waves and anisotropic turbulence occurs [e.g. Müller et al., 2005]. Theoretical knowledge suggests that the downscale energy cascade at this scale range is driven by internal wave breaking [Thorpe, 1987, Baines and Mitsudera, 1994; Riley and Lindborg, 2008]. Although different scenarios have been proposed to characterize this transition (fig. S1b), the scarce observational evidence favoring one or another makes discussions rather speculative. The fact that the cascade is intermittent in time and localized in space contributes to worsen the situation.

Consequently, mixing and dissipation are not formally incorporated in numerical ocean circulation models, but they are parametrized using eddy viscosity coefficients that are tuned a posteriori by fitting calculations with observations [e.g. Gregg et al, 1987; Ferrari and Wunsch, 2009]. This situation hampers the predictive capability of ocean circulation models for a number of phenomena, because a significant part of heat and salt mixing, which affect critically long-term climate evolution; or nutrient and pollutant dispersion, occur at these scales. Therefore, there is ample agreement on the fact that a first step towards improving model predictions is acquiring empirical knowledge on the mechanisms driving internal wave breaking and dissipation.

In this work, we present observational evidence indicating that the energy cascade in the Alboran Sea thermocline appears to follow the inertia-gravity-wave route, in which internal wave breaking is likely caused by Kelvin-Helmholtz (KH)-like shear instabilities. Our finding is based on the analysis of the horizontal wavenumber (k_x) spectra of the vertical displacements of acoustic reflectors corresponding to isopycnal surfaces imaged with a multi-scale HR-MCS system. In the rest of the manuscript, we first describe the characteristics of the acquisition system and the methods used to process and analyze the data, then we discuss the obtained results and we draw some general conclusions.

2 Study area and data acquisition system

The Alboran Sea is located in the westernmost Mediterranean. It is an oceanographically active area characterized by the exchange between Atlantic and Mediterranean waters across the Strait of Gibraltar (AW and MW, respectively, in fig. 1).

The water exchange creates a thermohaline stratification that, at the time of the HR-MCS data acquisition, was concentrated between 35 m and 110 m deep (AMW in fig. 1b). This stratified thermocline is known to be disturbed by internal waves mainly generated by barotropic tidal currents in the Strait of Gibraltar [Bruno et al., 2006; Vázquez et al., 2008] which then propagate into the Alboran basin, being scattered and reflected at the surrounding continental margins until they eventually break and dissipate. [e.g. Global Ocean Associates, 2002]. This situation, with the presence of a stratified and strongly sheared thermocline that is perturbed by internal waves, is theoretically prone to the development of different types of instabilities and stratified turbulence [Gregg, 1987]. The occurrence of either shear-type or convective instability depends critically on the thickness of the sheared layer. Shear instability takes place for waves with thinner interfaces, whereas convective instability dominates for waves with thick interfaces [Fringer and Street, 2003; Troy and Koseff, 2005]. In particular, KH instabilities could develop when the interface is thin and shearing is strong enough or stratification weak enough to bring the Richardson number, $R_i = N^2/|\partial V/\partial z|^2$, where N is the buoyancy frequency and $\partial V/\partial z$ is the variance of the vertical shear of the horizontal flow, below a critical value of 0.25 [Thorpe, 2005]. To calculate R_i within the targeted depth range of the Alboran AMW (30-110 m), we use $N(z) = \left(\frac{-\mathrm{g}}{\rho_0}\frac{\partial \rho(\mathrm{z})}{\partial \mathrm{z}}\right)^{\frac{1}{2}}$, where g is gravitational acceleration, ρ_0 is the mean density, and $\partial\rho(z)/\partial z$ is the density gradient obtained from one XCTD (see fig. 1 for location); and $\partial V/\partial z$ is estimated from local ADCP (Acoustic Doppler current profiler) data, which unfortunately are not simultaneous to the XCTD acquisition (SAGAS survey). The obtained value is $R_i=0.2\pm0.1$, so below the critical value (see additional details in table S1 and fig. S7). The combination of a set of conditions that are potentially prone to produce internal waves and wave instabilities, and an observational system with the appropriate resolution to resolve the horizontal spectrum, represents an extraordinary opportunity to identify and characterize the whole chain of events that allows transferring the energy between internal waves and turbulence.

The two HR-MCS profiles used in this work were acquired onboard the Spanish R/V Hespérides between May 16th and 19th, 2006, as part of the IMPULS (South Iberian Margin Paleoseismological integrated stUdy of Large active Structures) experiment. The characteristics of the acquisition system used in this experiment are described in the supplementary text S1. MCS systems are widely used in solid earth exploration and research, and they started to be used in oceanography following the preliminary results of Gonella and Michon [1988] and the seminal work of Holbrook et al. [2003], which opened a new branch in operational oceanography that has been called “seismic oceanography”. Subsequently, a series of studies have demonstrated the potential of conventional MCS data to image the thermohaline fine structure of the oceans [Biescas et al., 2008; Buffett et al., 2009; Sheen et al., 2012; Ménesguen et al., 2012], to extract water properties such as sound speed, temperature or salinity [Papenberg et al., 2009; Bornstein et al., 2013; Biescas et al., 2014; Padhi et al., 2015] or to provide information on internal wave dynamics and turbulence [Holbrook and Fer, 2005; Sheen et al., 2009; Krahmann et al., 2009; Falder et al., 2016], all with extraordinary detail in the horizontal dimension.

3 Data processing and analysis

3.1 MCS data processing

A processing flow specially designed to image the structure around the thermocline depth was applied to the HR-MCS IMPULS-2 and IMPULS-3 profiles (I2 and I3 in fig. 1a), using SEISMOS/ Western-Schlumberger and Seismic Unix software. It includes 2D geometry correction, CMP fold doubling to enhance signal-to-noise ratio (SNR), zero-phase band-pass frequency filtering between 40 Hz and 240 Hz to remove random background noise, amplitude correction to account for geometrical spreading, pre-stack time migration, application of a Karhunen-Loève transform filter with an eigenvalue cutoff ratio of 0.2 to mitigate direct wave amplitude, CMP sorting, normal move out correction, CMP stack, and finally post-stack depth conversion using the sound speed profile measured with XBTs that were deployed simultaneously to the seismic acquisition (fig. S2). The processed and depth-converted images corresponding to both profiles are shown in fig. 2. The seismic image is noisier for IMPULS-2. This is due to the faster shooting rate in IMPULS-2 (6 s between shots) than in IMPULS-3 (10 s), which means that coherent residual noise within the water layer arising from previous shots is higher.

3.2 Acoustic reflectors tracking

Despite the background noise, both profiles show clear, laterally continuous acoustic reflections within the depth range of the stratified thermocline (fig. 2). These reflectors are originated at the acoustic impedance contrasts that characterize the thermocline, essentially through temperature changes [Sallares et al., 2009]. As is explained in the supplementary text S2, lateral correlation-based SNR analysis confirms that the usable frequency band to track reflectors is 40-240 Hz (figs. S3, S4 and table S2). A total of 117 reflectors with lateral correlation lengths ≥1,250 m, were selected and automatically tracked using a criterion of maximum cross-correlation between adjacent traces (fig. S5), ensuring that all of them contribute equally to the slope spectra within the analyzed scale range. The depth range of the tracked reflectors in the two profiles is 30-100 m. Considering that lateral resolution of the HR-MCS system at the target's depth, which is limited by the width of the first Fresnel zone, $2R_x \approx (\lambda d)^{1/2}$, where d is the source-target distance and λ is the source wavelength, is 8-17 m (see additional details in table S1 and supplementary text S3), this data set provides continuous spectral coverage between 10^1 m and 10^3 m in the horizontal dimension.

3.3 Calculation of the k_x spectra

Fig. 3 displays the k_x spectra of the averaged vertical displacements of all the tracked reflectors, with their 95% confidence intervals (2σ). The approach to calculate the spectra is analogous to that followed in previous studies [Holbrook and Fer, 2005; Sheen et al., 2009; Holbrook et al., 2013], but we use a higher frequency source and focus on shallower targets, so lateral resolution improves. The individual power spectra of the tracked reflectors were calculated using the Fast Fourier Transform function of MATLAB and they were normalized by the number of points. Then the average spectrum of all reflectors was calculated, it was multiplied by $(2\pi k_x)^2$ to emphasize slope variations, and scaled by the buoyancy frequency (N/N_0). As suggested by Holbrook et al. [2013], we also calculated the slope spectrum directly from the seismic data. The resulting spectrum shows the same three spectral slopes at the same scales, although the slope changes are slightly more subdued. Random noise is identified at the highest wavenumbers. A k_x filter (stop band) was applied to remove the harmonic noise in each profile according to the shot distance, which is 15 m (66.67 km^{-1}) for IMPULS-2 and 25 m (40 km^{-1}) for IMPULS-3 (fig. S4).

4 Discussion of results

A key assumption when comparing the slope spectrum of vertical displacements with theoretical estimates of kinetic energy is that the undulation of acoustic reflectors reproduces indeed isopycnal displacements. This assumption is reasonable in regions that are not subject to salinity-temperature compensating intrusions [Biescas et al., 2014], as is the case of the Alboran thermocline. It is worth noting that the spectra of the two individual profiles show the same characteristics as the combined one (fig. S4), despite the fact that the vessel moved in opposite directions during the data acquisition, and that the time lapse between them was 10 hours. Therefore, it must reflect robust oceanographic features that are common in the two profiles, with negligible effects of water and vessel's motion [Klaeschen et al., 2009; Vsemirnova et al., 2009] and the images can be considered as quasi-synoptic for the scale range analyzed (supplementary text S4).

Overall, the obtained k_x spectrum displays three well-defined subranges characterized by contrasting spectral slopes (fig. 3). At the largest wavelengths of the analyzed scale range (1000 m>λ_x>100 m, where $\lambda_x=k_x^{-1}$), the energy decay follows a power law spectral density fall, k_x^{-q}, with q=2.05±0.06, which corresponds to the red line in fig. 3. The obtained slope coincides with the value predicted by the Garrett-Munk heuristic internal wave model ($q=2$) [Garrett and Munk, 1979], which has been observationally confirmed in a wide range of oceanic settings. Assuming Taylor's hypothesis, which allows relating temporal to spatial fluctuations in turbulent flows [Taylor, 1938], the horizontal scales corresponding to the local f_c and N, which define the limits of the internal wave subrange, are $l_c=2\pi\,\Delta V/f_c\approx 9.2$ km and $l_N=2\pi\,\Delta V/N\approx 91\pm 20$ m, respectively; where f_c is the Coriolis frequency at 36º, N is the buoyancy frequency as defined in section 2, and ΔV is the root mean square amplitude of the velocity fluctuation about the mean, which is also calculated within the targeted depth range (30-110 m) from the ADCP data (see additional details in table S1 and supplementary text S5). Interestingly, the slope change occurs at a scale that coincides -within error bounds- with the estimated l_N (fig. 3), upholding the idea that this scale actually limits the subrange controlled by gravity wave dynamics, in which most energy is carried by large amplitude, long-wavelength internal waves. To visualize the features that contribute to this part of the spectrum, we have band-pass filtered between 5000 m and 100 m the two horizons highlighted in red and blue in fig. 2. The resulting structures (fig. 4a,c) are compatible with IWs, having amplitudes that range from ~10 m for the largest ones (λ_x>10^3 m) to a few meters for the smallest ones ($\lambda_x\approx l_N$).

The observational gap is particularly pronounced below l_N, so the knowledge on the processes governing the transition between anisotropic and isotropic motions that must occur at this scale is not based on observations. Theory and models indicate that the transitional subrange associated to KH-instabilities and stratified turbulence should display a spectral roll-off near l_N, marking the point where dissipative effects overcome the stability that dominates at larger scales [Gregg, 1987; D'Asaro and Lien, 2000; Carnevale et al., 2001]. In particular, high-resolution numerical experiments give a q value of 2.5-3.1 [Waite, 2011]. This is consistent with the spectral slope of q=2.8±0.2 obtained between l_N and $l_s\approx 33\pm 4$ m from the tracked horizons (fig. 3). The features that contribute to this spectral subrange for the blue and red horizons of fig. 2 are shown in fig. 4b,d.

The likely presence of KH billows in the Mediterranean thermocline was first shown by dye tracing experiments performed around Malta [Woods, 1968]. However, one of the clearest recent observational evidence corresponds to a KH billow train imaged with a thermistor chain in a downslope tidal flow above the sloping side of the Great Meteor Seamount, Canary Basin [van Haren and Gostiaux, 2010; Smyth and Moum, 2012]. These data show a rough, wavy horizon displaying a series of spikes with amplitudes of 1-5 m and wavelengths of 50-75 m. Even if both the depth and oceanographic setting of this experiment differs from ours, it is worth noting that the features identified as KH billows are consistent with those contributing to the transitional subrange in our data (fig. 4b,d). Another distinctive hallmark of KH billows is a wavelength, l, one order of magnitude larger than the thickness of the sheared layer, δ, which marks in turn the maximum size of the fastest growing disturbances [e.g. Smyth and Moum, 2012]. Our observations suggest a rather complex situation, certainly more than in lab and numerical experiments. First, the transitional subrange, which we interpret to represent KH billows (fig. 4), covers a range of scales -hence possible values of l- between ~100 m and ~30 m. Second, the thickness of the sheared layers, as defined by the vertical separation between contiguous reflectors, is also variable (δ=13±3 m). If we assume that the point of slope breaking towards the transitional domain ($\lambda_x \approx 100 \pm 20$ m) marks the wavelength of the greatest disturbances, we obtain $l/\delta = 100/13 \approx 7.5$, similar to what was originally described for KH billows in a steady flow [Miles and Howard, 1964]. However, the range of possible values for both δ and l prevents any general interpretation or conclusion concerning the value of l/δ. Similarly, it has been shown that the prevalence of KH-type instability depends critically value $k\delta$, where $k=2\pi/\lambda$ and λ is the wavelength of the internal wave [Fringer and Street, 2003]. When $k\delta<0.56$, the most unstable wavelength associated with a shear instability is small enough to grow at the interface and develop KH billows, but it is not energetic enough to induce convective instability. For the values described above, we obtain $k\delta<0.5$, providing additional support to the presence of KH instabilities. However, as in the case of l/δ, there is a range of possible values for k and δ that makes difficult a direct, univocal comparison with experimental results.

While the onset of KH-instabilities at l_N is reproduced by numerical simulations, the scale of transition to turbulence is unclear. In the obtained spectrum, the slope changes to $q \approx 1.64$ at $l_s \approx 33 \pm 4$ m (fig. 3). This slope is close to the q=5/3 predicted by the Batchelor's model [Batchelor, 1959], which describes the energy continuum of the turbulent inertial subrange. This coincidence suggests that the smallest billows have collapsed and dynamics starts to be dominated by turbulence at l_s. This scale is one order of magnitude larger than the local Ozmidov length scale, $l_o \approx 2 \pm 1$ m (table S1 and supplementary text S5), suggesting that the transition does not reflect the transition to isotropic turbulence but rather to stratified turbulence. The smallest scale that is resolved with the HR-MCS system, as indicated by the slope change to $q \approx 0$, characteristic of white noise, is $l_n \approx 15$ m (fig. 3), a value consistent with the nominal lateral resolution of the system (table S1).

In summary, the spectral analysis of the multi-scale HR-MCS data allows characterizing the sequence of events that drives the energy cascade between internal waves and turbulence in the Mediterranean thermocline. Our interpretation is that transition starts with the development of KH-instabilities, which first capture the internal wave energy along the stratified thermocline near l_N, and then they transfer it to the turbulent scale after collapsing near l_s.. Even though our analysis is local, the fact that the averaged spectrum displays the transitional subrange indicates that KH-billows are ubiquitous in the area, so this chain of events is taking place continuously and simultaneously, with each process occurring at and affecting to a specific scale range.

As stated in the introduction, current knowledge on the mechanisms governing the energy transfer at the sub-mesoscale is rather poor mainly due to the lack of observational systems providing observations at the appropriate range of scales. This makes that small-scale phenomena are not formally incorporated in numerical ocean circulation models, hindering their predictive capability in scenarios where mixing and dissipation are important. The availability of an observational system that can cover this observational gap could possibly help mitigating this issue. Additionally, it must be noted that, in contrast to the conventional heavy, fixed, limited-resolution MCS systems used in previous experiments, the HR-MCS ones are relatively light and portable, and so they can be readily installed and operated in mid-size oceanographic vessels. This fact, combined with the better resolution that provides the higher-frequency source, opens new perspectives in oceanographic research at the sub-mesoscale.

5 Conclusions

The spectral analysis of the vertical displacements of acoustic reflectors at thermohaline boundaries using data acquired with a multi-scale, HR-MCS system provides observational evidence indicating that the energy cascade between meso-scale and small-scale motions in the Alboran Sea thermocline is driven by the development of internal wave shear instabilities of the Kelvin-Helmholtz-type. In particular, our results show that ocean dynamics at the thermocline depth is dominated by internal waves at scales larger than the horizontal buoyancy scale, $l_N \approx 91$ m, below which shear instabilities of the KH-type develop until they collapse at $l_s \approx 33$ m, giving rise to turbulence. These observations shed new light on the mechanisms and routes of energy transfer between internal waves and turbulence in the thermocline. Even if our study is local, the availability of a relatively light, portable system providing observations at the appropriate scales opens new perspectives to improve our knowledge on mixing and dissipation.

Acknowledgments

We thank J.L. Pelegrí, and P. Puig for reading early versions of the manuscript, M. Bruno for critical review of the work, and all colleagues at Barcelona-CSI for advice and support. Data are available under request to the first author. This work has been done in the framework of projects POSEIDON (CTM2010-25169), APOGEO (CTM2011-16001-E/MAR), both funded by the Spanish MINECO. The seismic and oceanographic data were acquired during the IMPULS (CTM2003-05996-MAR) and SAGAS (CTM2005-08071-C03-02/MAR) surveys also from MINECO. Third author's work has been supported by the European Commission through OCEANSEIS project (Marie Curie Action FP7-PEOPLE-2010-IOF-271936) and Marie Curie Action FP7-PEOPLE-2012-COFUND-600407.

References

Baines, P. and H. Mitsudera (1994), On the mechanism of shear flow instabilities, J. Fluid Mech., 276, 327–342.

Batchelor, G. K. (1959), Small-scale variation of convected quantitites like temperature in turbulent fluid, J. Fluid Mech., 5, 113–139.

Biescas, B., V. Sallares, J.L. Pelegrí, F. Machin, R. Carbonell, G. Buffett, J.J. Dañobeitia and A. Calahorrano (2008), Imaging meddy finestructure using multichannel seismic reflection data, Geophys. Res. Lett., 35, L11609, doi:10.1029/ 2008GL033971.

Biescas, B., et al. Recovery of temperature, salinity and potential density from ocean reflectivity. J. Geophys. Res., 119, 3,171–3,184 (2014).

Bornstein, G., B. Biescas, V. Sallares, and J. F. Mojica (2013), Direct temperature and salinity acoustic full waveform inversion, Geophys. Res. Lett., 40, 4344–4348, doi:10.1002/grl.50844.

Bruno, M., et al. (2006), Observations of internal waves and associated mixing phenomena in the Portimao Canyon area, Deep Sea Res. II, 53, 1,219-1,240.

Buffett, G., B. Biescas, J.L. Pelegrí, F. Machín, V. Sallares, R. Carbonell, D. Klaeschen and R. Hobbs (2009), Seismic reflection along the path of the Mediterranean undercurrent, Cont. Shelf Res., 29, 1848–1860.

Carnevale, G.F., M. Briscolini and P. Orlandi (2001), Buoyancy- to inertial-range transition in forced stratified turbulence, J. Fluid Mech., 427, 205-239.

D'Asaro, E.A. and R.C. Lien (2000), Lagrangian measurements of waves and turbulence in stratified flows, J. Phys. Oceanogr. 30, 641–655.

Falder, M., N.J. White, and C.P. Caufield (2016), Seismic imaging of rapid onset of stratified turbulence in the South Atlantic ocean, J. Phys. Ocean., 46, 1023-1044, doi: 10.1175/JPO-D-15-0140.1.Ferrari, R., and C. Wunsch (2009), Ocean circulation kinetic energy: reservoirs, sources and sinks, Annu. Rev. Fluid Mech., 41, 253-282,
doi: 10.1146/annurev.fluid.40.111406.102139.

Fringer, O.B., and R.L. Street (2003), The dynamics of breaking progressive interfacial waves, J. Fluid Mech., 494, 319–353, doi:10.1017/S0022112003006189.

Garrett, C. and W. Munk (1979), Internal waves in the ocean, Ann. Rev. Fluid Mech., 11, 339-369.

Global Ocean Associates, Office of Naval Research (2002), An Atlas of oceanic Internal Solitary Wave; The Strait of Gibraltar, Code 322PO.
http://www.internalwaveatlas.com/Atlas_PDF/IWAtlas_Pg099_StraitGibraltar.PDF

Gonella, J., and D. Michon (1988), Deep internal waves measured by seismic reflection within the eastern Atlantic water column, C. R. Acad. Sci., Ser. II, 306, 781–787.

Gregg, M.C. (1987), Diapycnal mixing in the thermocline: A review, J. Geophys. Res., 92, 5,249–5,286.

Holbrook, W.S., P. Páramo, S. Pearse and R.W. Schmitt (2003), Thermohaline fine structure in an oceanographic front from seismic reflection profiling, Science, 301, 821-824.

Holbrook, W.S. and I. Fer (2005). Ocean internal wave spectra inferred from seismic reflection transects, Geophys. Res. Lett., 32, L15604.

Holbrook, W.S., et al. (2013), Estimating Oceanic Turbulence Dissipation from Seismic Images, J. Atmos. Oceanic Technol., 30, 1767–1788.

Klaeschen, D., R.W. Hobbs, G. Krahmann, C. Papenberg and E. Vsemirnova (2009), Estimating movement of reflectors in the water column using seismic oceanography, Geophys. Res. Lett., 36, L00D03.

Krahmann, G., P. Brandt, D. Klaeschen and T. Reston (2008), Mid-depth internal wave energy off the Iberian Peninsula estimated from seismic reflection data, J. Geophys. Res., 113, C12016, doi:10.1029/2007JC004678.

McComas, C.H. and F.P. Bretherton (1979), Resonant interaction of oceanic internal waves, J. Geophys. Res., 82, 1397–412.

Ménesguen, C., B. Hua, X. Carton, F. Klingelhoefer, P. Schnurle and C. Reichert (2012), Arms winding around a Meddy seen in seismic reflection data close to the Morocco coastline, Geophys. Res. Lett., 39, L05604, doi:10.1029/2011GL050798.

Miles, J. W., and L. N. Howard (1964), Note on a heterogeneous shear flow. J. .Fluid Mech., 20, 331-336, doi:10.1017/S0022112064001252

Müller, P., J. McWilliams and M. Molemaker (2005), Routes to dissipation in the ocean: the two-dimensional/three-dimensional turbulence conundrum, in Marine turbulence, observations and models. Results of the CARTUM project, H.Z. Baumert, J. Simpson, J. Sündermann, Eds. Cambridge University Press, Cambridge, UK.

Padhi, A., S. Mallick, W. Fortin, W.S. Holbrook and T. Blacic (2005), 2-D ocean temperature and salinity images from pre-stack seismic waveform inversion methods: an example from the South China Sea, Geophys. J. Int., 202 (2): 800-810, doi:10.1093/gji/ggv188.

Papenberg, C., D. Klaeschen, G. Krahmann and R. Hobbs (2010), Ocean temperature and salinity inverted from combined hydrographic and seismic data, Geophys. Res. Lett., 37, L04601, doi:10.1029/2010GL042115.

Riley, J. and E. Lindborg (2008), Stratified turbulence: A possible interpretation of some geophysical turbulence measurements, J. Atm. Sci., 65, 2,416-2,424.

Sallares, V., et al. (2009), Relative contribution of temperature and salinity to ocean acoustic reflectivity, Geophys. Res. Lett., 36, L00D06, doi:10.1029/2009GL040187.

Sheen, K. L. N.J. White and R.W. Hobbs (2009), Estimating mixing rates from seismic images of oceanic structure, Geophys. Res. Lett., 36, L00D04, doi: 10.1029/2009GL040106.

Sheen, K.L., N.J. White, C.P. Caulfield and R.W. Hobbs (2012), Seismic imaging of a large horizontal vortex at abyssal depths beneath the Sub-Antarctic Front, Nature Geosc., 5, 542–546, doi:10.1038/ngeo1502.

Sheriff, E.G. and L.P. Geldart (1995), Exploration Seismology (2nd ed.), Ed. Cambridge University Press, Cambridge, UK.

Smyth, W. and J. Moum (2012), Ocean mixing by Kelvin-Helmholtz instability, Oceanography, 25, 140-148.

Taylor, G. I. (1938), The spectrum of turbulence, Proc. R. Soc. London A, 164, 476.

Thorpe, S.A. (1987), Transition phenomena and the development of turbulence in stratified fluids, J. Geophys. Res., 92, 5,231–5,245.

Thorpe, S.A. (2005), The Turbulent Ocean, Cambridge Univ. Press., Cambridge, UK.

Troy, C.D., and J.R. Koseff (2005), The instability and breaking of long internal waves, J. Fluid. Mech., 543, 107-136, doi:10.1017/S0022112005006798.

Van Haren, H., and L. Gostiaux (2010), A deep-ocean Kelvin-Helmholtz billow train, Geophys. Res. Lett., 3 7, L03605, doi:10.1029/ 2009GL041890.

Vázquez A., M. Bruno, A. Izquierdo, D. Macias and A. Ruiz-Cañavate (2008), Meteorologically forced subinertial flows and internal wave generation at the main sill of the strait of Gibraltar, Deep-Sea Res. I, 55, 1,277 - 1,283.

Vsemirnova, E., R. Hobbs, N. Serra, D. Klaeschen and E. Quentel (2009), Estimating internal wave spectra using constrained models of the dynamic ocean, Geophys. Res. Lett., 36, L00D07, doi:10.1029/2009GL039598.

Waite, M.L. (2011), Stratified turbulence at the buoyancy scale, Phys. Fluids, 23, 066602.

Woods, J. (1968), Wave-induced shear instability in the summer thermocline, J. Fluid Mech., 32, 791–800.

Yilmaz, O. (2001), Seismic Data Analysis: Processing, Inversion and Interpretation of Seismic Data, Ed. Society of Exploration Geophysics, Houston, TX.

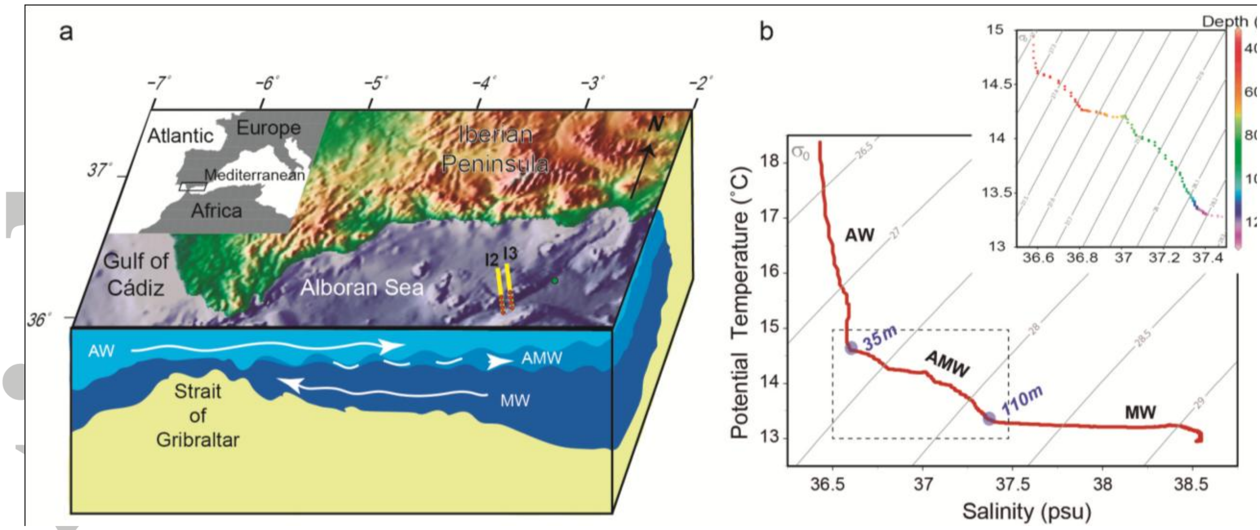

Figure 1. (a) Bathymetric map of the Alboran Sea and location of the data used in the study: HR-MCS profiles acquired during the IMPULS-2006 experiment (yellow lines labelled I2 and I3), eXpendable Bathy-Thermograph (XBTs) profilers (red circles), eXpendable Conductivity/ Temperature/ Depth (XCTD) probe (green circle). Sketch of the different water masses in the study region and their relative motion. Abbreviations: Atlantic Water (AW), Atlantic Modified Water (AMW) and Mediterranean Water (MW). Blue circles indicate transition depths. **(b)** Temperature-Salinity diagram from the XCTD probe, σ_0 is potential density in kg/m^3. The dashed rectangle indicates the zoomed area in the inset.

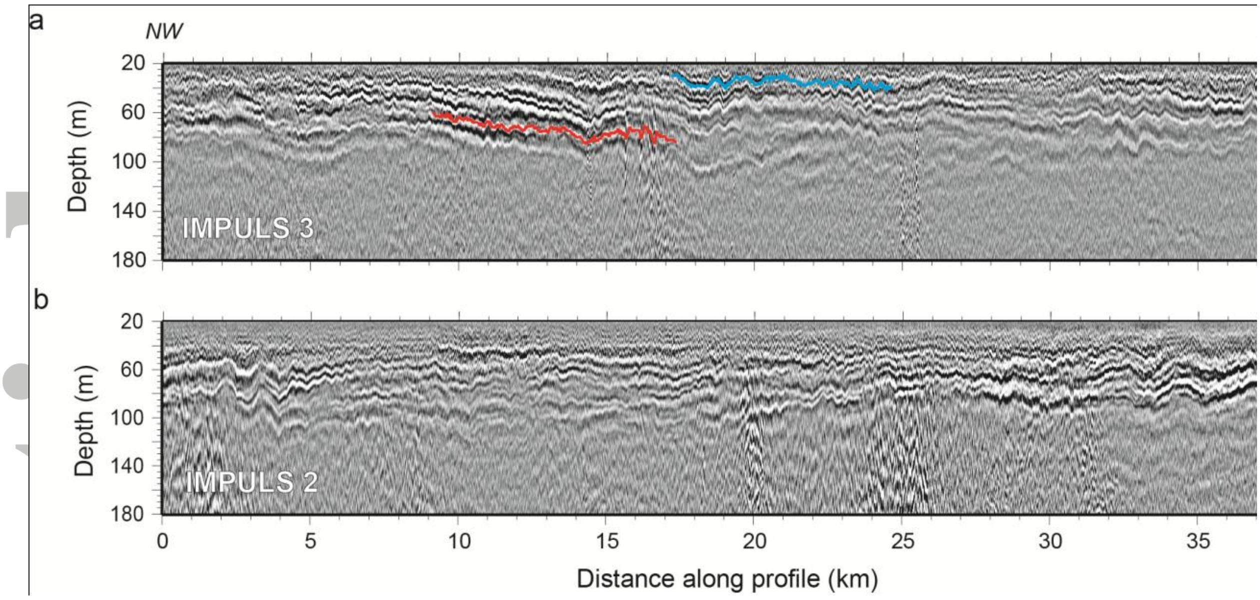

Figure 2. Seismic record sections corresponding to HR-MCS profiles IMPULS-3 **(a)** and IMPULS-2 **(b)** (I3 and I2, respectively, in fig. 1a). The data have been processed to improve shallow water imaging and depth-converted using an XBT-derived sound speed model (fig. S2). The red and blue lines correspond to the two tracked horizons analyzed in fig. 4.

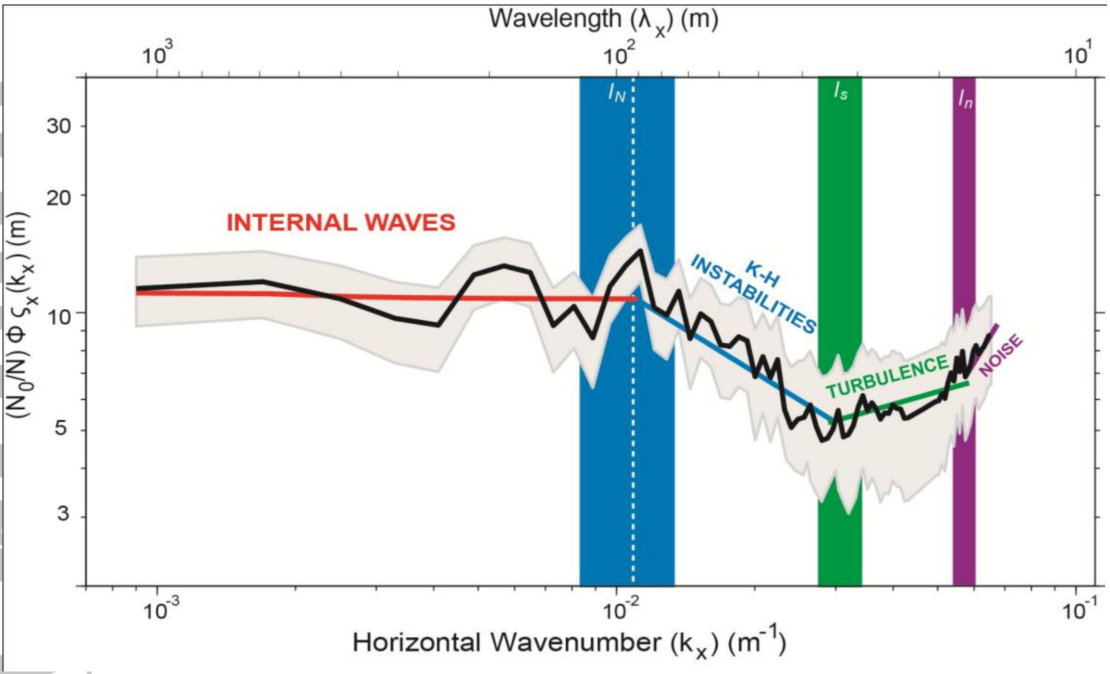

Figure 3. Average horizontal spectrum of the vertical displacement of the 117 tracked reflectors (ϕ_{Rx}) scaled by the local buoyancy frequency at the reflector depth (N_0/N) to eliminate stratification effects, and multiplied by $(2\pi k_x)^2$ to enhance slope variations (black line), and its 95% confidence interval (grey shaded area). The reference lines follow theoretical slopes of Garrett-Munk internal wave (IW) model [Garrett and Munk, 1979] (red line), Kelvin-Helmholtz instabilities [Waite, 2011] (blue line), and Batchelor's model for turbulence [Batchelor, 1959] (green line). The violet line is white noise. The blue rectangle marks the slope change between IWs and KH subranges, whereas the dashed white line labelled l_N indicates the horizontal buoyancy scale calculated from oceanographic data (table S1 and supplementary text S5). The green rectangle labelled l_s indicates the limit between transitional and turbulent subranges, and the violet one labelled l_n marks the incidence of noise. The width of these rectangles indicates the uncertainty in the determination of the slope change (i.e. the standard deviation of the slope change determined in all the individual horizons).

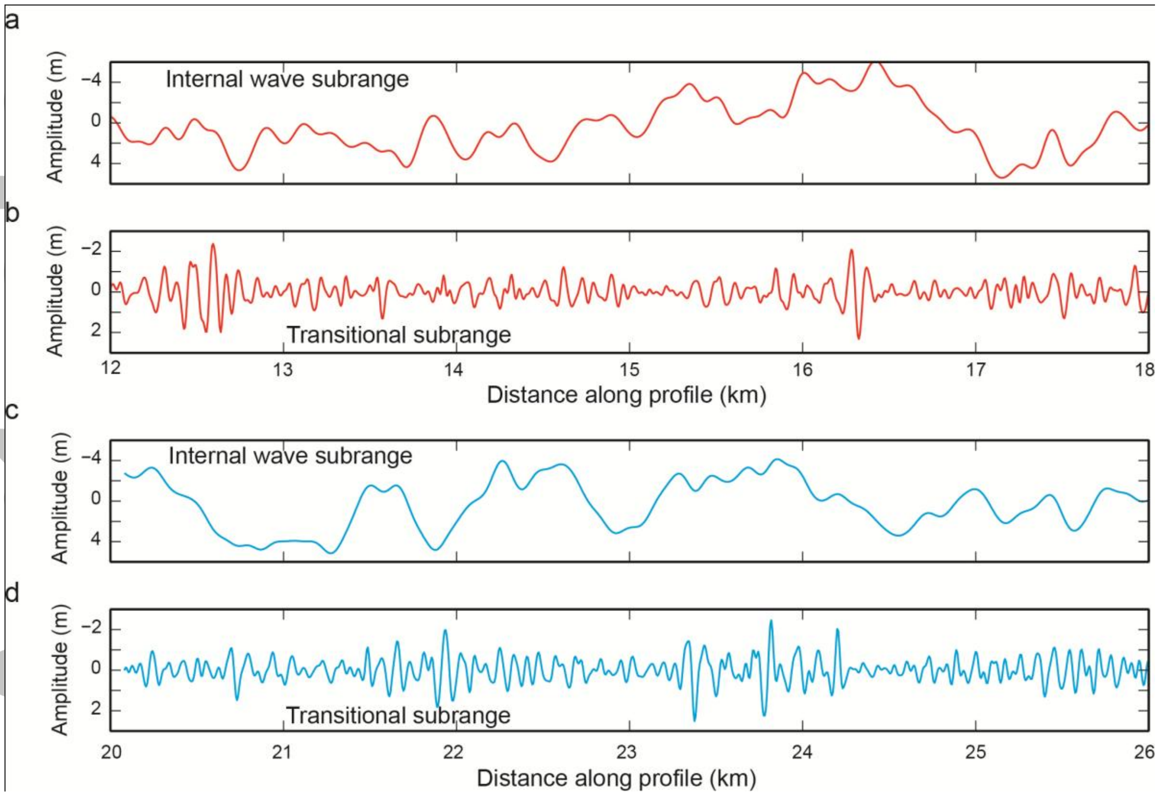

Figure 4. Band-pass filtered reflectors corresponding to the red and blue horizons highlighted in fig. 2. Signal in panels (a) and (c) has been filtered between 5000 m and 100 m, which correspond to the IW subrange in fig.3. Signal in panels (b) and (d) has been filtered between 100 m and 30 m, which correspond to the transitional subrange (KH instabilities in fig. 3).